ESIA15 & ISSI-2019 Joint Conference on
Engineering Structural Integrity Assessment

COMPARING TECHNIQUES FOR QUANTIFICATION OF CREEP CAVITIES

Siqi He[1,*], Peter E J Flewitt[1,2], David M Knowles[3], Tomas Martin[1]

Creep cavitation is a key limitation for the life of a component acting under load at elevated temperatures. This paper compares several modern techniques available to characterize and understand the formation of creep cavities. Conventional 2D imaging techniques such as Scanning Electron Microscopy (SEM) and Focused Ion Beam (FIB) imaging characterize morphology and distribution over a large area, while scanning transmission electron microscopy (STEM) has higher resolution but limited sampling area. 3D imaging techniques such as X-ray Tomography (XRT) enable the characterization of creep cavities in three dimensions, however XRT can be limited in cavity identification due to resolution. To bridge the length-scale gap, FIB serial sectioning can reconstruct the creep cavities at a single grain boundary with a much higher resolution, whilst advancements in Plasma FIB enable this high resolution characterization over a larger reconstruction volume. For optimum creep cavitation characterization, multiple techniques should be used in complement with each other.

INTRODUCTION

The Advanced Gas-Cooled Nuclear Reactors (AGRs) used in the UK are approaching their designed lifetime. To fill the 'energy gap' created by the reduction of traditional fossil fuel plants [1] and during new nuclear power station construction, there is a need to extend the operating lifetime of these AGRs. Intergranular creep cavitation is an important degradation mechanism for austenitic stainless steel components operating at elevated temperature such as AGR boiler headers. Quantifying the initiation and growth of creep cavities is required to understand the underlying mechanisms. Although much work has been undertaken to quantify creep damage, over the past decades several improved techniques have been developed [2]–[6]. For example, electron backscatter diffraction (EBSD) was used by Warren [1] to find the association between creep cavities and secondary bcc phases in AISI 316H stainless steel. Also Chen et al. [7] investigated the correlation between cavities and carbide precipitates with the use of focused ion beam (FIB) milling and imaging. 3D visualization techniques provided an improved measure of spatial distribution and volume fraction of cavities. Gupta et al. [8] and Burnett et al. [9] used X-ray Tomography (XRT) with a synchrotron X-ray source to study the creep cavitation in martensitic steel and 316 stainless steel respectively, while Daly et al. [10] adopted X-ray tomography combined with Plasma FIB (PFIB) dual beam sectioning 3D reconstruction to investigate plastic voids. In this paper, we compare the capability of

[1]Interface Analysis Centre, H.H. Wills Physics Laboratory, University of Bristol, Bristol, BS8 1TL, UK
[2]School of Physics, H.H Wills Physics Laboratory, University of Bristol, Bristol, BS8 1TL, UK
[3]Solid Mechanics Group, Department of Mechanical Engineering, University of Bristol, Bristol, BS8 1TR, UK
[*]Corresponding author. E-mail address: siqi.he@bristol.ac.uk

various high spatial resolution techniques to characterize creep cavitation in post-service austenitic steel header samples.

EXPERIMENTAL DETAILS

Two AISI 316H stainless steel specimens were cut from an AGR boiler header. The nominal composition of the steel is shown in table 1. Both specimens served at a temperature of 490 °C to 530 °C for 65000 hours. The first sample had no post-service heat treatment, whilst the second sample had 22000 hours post-service aging at 550 °C.

Table 1: The nominal composition of the ex-service cast 69431 AISI 316H stainless steel (wt%)

C	Si	Mn	P	S	Cr	Mo	Ni	B	Co	Fe
0.06	0.4	1.98	0.021	0.014	17.17	2.19	11.83	0.005	0.1	66.23

The specimens were ground and polished using silicon carbide papers to a finish of 0.25 µm, and were then further polished in colloidal silica. A Zeiss Sigma FEG-SEM was used to perform the Scanning Electron Microscopy (SEM) and EBSD analysis. EBSD maps were collected by the software OIM, at an accelerating voltage of 30 kV and aperture size of 120 µm to improve the signal-to-noise ratio [11]. A FEI Helios NanoLab 600i Dualbeam was used for Transmission Electron Microscopy (TEM) thin foil lift-out and conventional dual beam cross-sectioning. A TEM thin foil across a grain boundary was prepared with the Ga ion beam current decreased in steps during thinning to achieve a final thickness of ~100 nm, before further polishing with a low energy ion beam (5 kV) to remove the prior surface damage from the thinning. Finally, the specimen was moved from the trench onto a copper grid using a micro-manipulator on an optical microscope. The TEM diffraction patterns were obtained from a Philips EM430 TEM operated at a voltage of 200 kV whereas the STEM dark field (DF) imaging was taken from a JEOL ARM-200F TEM operated at 200 kV.

Dual beam cross-sectioning was obtained by FEI Auto Slice and View software. A total number of 100 slices of nominal 0.2 µm thickness were milled at 30 kV, 6.5 nA in series. The secondary electron images were recorded at 15 kV and 0.69 nA using an Everhart-Thornley detector, giving a voxel size of 0.017 × 0.021 × 0.2 µm. To investigate XRT for characterizing creep cavitation for size and distribution, a small section was cut from the ex-service sample and imaged using a Zeiss Xradia 520 Versa X-ray microscope, operating with a voltage of 160 kV, voxel size of 0.87 µm and an exposure time of 40 seconds. The plasma FIB cross-section was performed with a ThermoFisher Helios G4 PFIB using a 30kV 60nA Xe ion beam across a 130 × 62.7 µm area and 209 slices each at 300 nm thickness. Images were taken automatically after each slice using a SEM-CBS detector at a tilt of 54° at 5 kV and 1.6 nA with a pixel size of 36.3 nm.

All 3D imaging data was processed on Avizo 9.7.0 software. For the conventional dual beam cross-sectioning, the slices were manually aligned. A background detection correction filter was used to remove shadows and uneven illumination, and a fast fourier

transform (FFT) filter removed the curtaining and any associated blurring was then corrected using an unsharp masking filter. An edge-preserving smoothing removed noise before final segmentation. The segmentation was performed with global greyscale threshold with very limited manual works on corrections of several slices. The data processing for XRT and PFIB have been described in detail by Daly et al. [10]. In this work, edge-preserving filter and median filter were used for XRT data. A watershed tool removed the background and retained material section. Global threshold and 'top hat' tools were then used to segment the cavities and inclusions. For the PFIB data, the FFT, unsharp masking, edge-preserving and median filter was used in sequence, with the segmentation performed using greyscale threshold and 'top hat' tool [10].

RESULTS

Here we consider the capability of 2D and 3D techniques for evaluating the initiation and growth of creep cavitation in the ex-service type 316H header materials.

Two-dimensional imaging techniques

Figure 1a shows SEM examination of the specimen surface, indicating the presence of inclusions within the grain identified as MnS by Energy Dispersive X-ray (EDX). The grain boundaries display cavitation initiated during service. In Figure 1b, the creep cavities at the grain boundary have an irregular shape. Figure 1c and 1d show FIB secondary imaging, with strong grain contrast. For SEM secondary electron imaging, due to the low voltage used and relatively low average atomic number of the sample, topographic contrast dominates. For FIB imaging, topographic, channeling and material contrast all contribute, and comparing figure 1b and 1d shows a better topographic and morphological description of cavities in the SEM imaging. More detailed comparisons of secondary electron yield and channeling effect of ions and electrons have been described by Ishitani and Tsuboi [12], and Giannuzzi and Michael [13].

To investigate the relationship between creep cavitation and secondary phases, electron backscatter diffraction (EBSD) was performed. Figure 2 shows EBSD phase mapping indicating that the matrix of the material is austenite, with bcc phase particles homogeneously distributing at the austenite-austenite grain boundaries. Figure 2b shows that cavities are closely linked to bcc phase at the grain boundary. As reported by Warren [1], the ex-service + 22000 hours post aging can lead to chi and α-ferrite phase formation. The efficiency of secondary bcc phase identification was significantly reduced when austenite, chi and ferrite phase were included in the EBSD scanning simultaneously (i.e. a lower confidence index of chi and/or ferrite phase compared to detecting each individually). Therefore, only austenite and ferrite Kikuchi pattern datasets were selected. However, there is a possibility that the bcc phase is partly chi-phase.

To study the correlation between creep cavity and carbides precipitates, XeF_2 etching was performed within the FIB workstation to reveal the grain boundaries and precipitates. Figure 3a and 3b shows secondary electron images of the specimen before and after XeF_2 etching. After etching, the channeling contrast of the matrix grains reduced while the contrast of the grain boundary significantly increased. Figure 3c shows a higher

magnification image revealing fine intra-granular carbides precipitates and correlation between cavities and coarse carbides at the grain boundary. Liu et al. [21] account this contrast mechanism during XeF_2 etching to a reduction in the work function of the materials that increases secondary electron yield.

The bcc phase identified by EBSD was examined by STEM and TEM using a cross-section thin foil at a grain boundary. Figure 4a shows the STEM dark-field (DF) image of the thin foil with a mixed contrast arising from thickness, diffraction and atomic number (15 cm camera length used). A cavity and a secondary phase originating at the grain boundary are located on either side of the austenite-austenite grain boundary. The secondary phase was identified to have a bcc crystal structure with a lattice parameter of 2.92 Å by selected area electron diffraction patterns (SAED), which corresponds well with ferrite. One of the zone axis patterns of the bcc ferrite is shown in figure 4b. The longest axis of the ferrite was determined to be parallel to <110> crystal direction that corresponds with a fast growth direction.

Three-dimensional imaging techniques

Figure 5a shows the 3D reconstruction of the XRT scanning volume of the specimen, giving a total sampling volume of 804 µm length, 110-400 µm width and 800 µm height with a voxel size of 0.87 µm. Based on the attenuation contrast of the XRT, the features which have a lower X-ray attenuation than the austenite matrix were segmented as shown in figure 5a. The dominant feature is a mix of inclusion and associated smaller voids, with a relatively large size and a rod-like or ellipsoidal morphology. These features tend to be discrete and parallel with each other in the longest axis. The inclusions were identified to be manganese sulphide by EDX. In addition, some smaller segmented features can also be seen in figure 5a, which could be small inclusions, grain boundary cavities and/or second phases, but are not clearly distinguishable. Figure 5b is a FIB secondary electron imaging showing a void at the inclusion-matrix interface likely formed during in-service aging. To compensate for the resolution limitation of the XRT, conventional Ga^+ dual beam cross sectioning was performed for comparison as shown in figure 6. One frame of the serial slices is shown in figure 6a. Sub-surface cavities can be seen on the trench wall distributing at the grain boundary. Figure 6b shows FIB 3D reconstruction of the creep cavities. The cavities have an irregular shape in three dimensions. To compensate for the small sampling volume resulted from low Ga ion milling rate whilst maintaining the high spatial resolution, Xe^+ Plasma FIB sectioning was performed. Figure 7 is one frame of the PFIB serial sectioning showing the presence of cavities and retained δ-ferrite region.

CONCLUDING COMMENTS

The comparison of 2D techniques (SEM, FIB and STEM) for quantitative evaluation of creep cavitation is shown in table 2. The area of view was calculated as the horizontal field width (HFW) multiplied by the vertical field width (zero degrees tilt angle assumed). The minimum observable cavity size was defined as the equivalent circle diameter for approximatively nine times the pixel area (e.g. 3×3 pixels), as 2×2 pixels examples such as the marked feature in figure 8b are not clear enough to be identified as

cavities. The contrast, signal to noise ratio, sample surface condition, etc. could significantly affect the minimum number of pixels needed to distinguish the cavity.

When viewing cavities in the SEM, resolution is controlled by (1) the operating condition of the instrument, (2) the type of material and (3) the surface preparation. The ultimate resolution achievable could be as small as 5-10 nm [14]. For the FIB secondary electron imaging, despite introducing damage on the specimen surface, FIB imaging can provide a good ultimate resolution (10 nm) [15] whilst giving crystallographic information resulting from the channeling effect of ions. The dark regions on the FIB image (figure 1c) indicate a greater penetration depth resulting in fewer secondary electrons excited in the near-surface volume and a lower sputtering rate [16]. Three typical magnifications of SEM and FIB imaging are shown in table 2. Both SEM and FIB secondary imaging provide the direct observation of cavitation over a wide range of size. Due to a smaller probe size and absence of scattering signal from bulk specimen, the ultimate resolution for thin foils examined by STEM can be as small as 0.2 nm [17]. Although the high resolution of STEM enables the study of smaller cavities compared to SEM, the specimen area investigated is much smaller. In addition to the direct observation and quantification of cavities by SEM, FIB and STEM, EBSD could be used for investigating the secondary phase distribution, XeF_2 etching for carbides precipitate distribution, EDX for elemental distribution, and TEM for phase identification, lattice mismatch and dislocation density.

Table 2: The comparison of capabilities between 2D imaging techniques for creep cavitation

Technique	Ultimate resolution (nm)	Pixel resolution	Magnification	Area of view (μm^2)	Minimum observable cavity size (μm)
SEM	5-10 [14]	1024×768	200X	1.7×10^6	5
			1000X	6.8×10^4	1
			20000X	170	0.05
FIB	10 [15]	1024×943	200X	1.5×10^6	4
			1000X	6×10^4	0.8
			20000X	150	0.04
STEM	0.2 [17]	512×568	50000X	15	0.024
			200000X	1	0.006

The comparison of 3D imaging techniques (Ga^+ FIB serial sectioning, Xe^+ PFIB serial sectioning and XRT) for characterizing creep cavitation is shown in table 3. Due to the variable width (110-400 μm) of the XRT specimen, the nominal sampled volume was calculated using an average width of 255 μm. In [18], the spatial resolution of XRT

was estimated as twice the voxel size, and in [10], three to four times the voxel size. In this work, the spatial resolution of XRT was defined as the equivalent spherical diameter for approximately 8 times the voxel volume (i.e. 2×2×2 voxels). For comparison with XRT, the spatial resolution for Ga^+ FIB serial sectioning and Xe^+ PFIB serial sectioning was also defined as 2×2×2 voxels.

The XRT data in this work had a voxel size of 0.87 µm, giving an approximate spatial resolution of 4.6 µm. At this resolution, it is not possible to distinguish creep cavities from inclusions and grain boundary second phases by XRT, and smaller cavities can be missed, which can lead to incorrect measurements of the size distribution and volume fraction of the creep cavities. The spatial resolution of the Ga^+ FIB serial sectioning tomography is much higher than the XRT which can lead to the visibility of small cavities shown in figure 6b. However, FIB has a significantly smaller nominal sampling volume ($20 \times 10 \times 20$ µm^3), due to the smaller voxel size ($0.017 \times 0.021 \times 0.2$ µm). Due to the high spatial resolution, the Ga^+ FIB cross sectioning is able to separate individual cavities from each other, enabling the study of the morphology of each cavity individually and investigation the size distribution and volume fraction accurately. For the Xe^+ PFIB, an estimated spatial resolution of 0.4 µm is achieved, while the reconstructed volume is larger than conventional FIB sectioning, giving $92 \times 37 \times 57$ µm^3 in size. The rocking mill technique in the PFIB, where the ion beam is oriented at two different rocking angles during cross-sectioning, can reduce curtaining during the milling. Because of the complex contrast resulted from high current milling damage, significant channeling contrast, etc., the cavities were not completely segmented in the PFIB data. Here some carbide precipitates could be incorrectly identified as cavities as a result of similar contrast between these precipitates and cavities in the PFIB.

Table 3: The comparison of capabilities between 3D imaging techniques for creep cavitation

Technique	Ultimate voxel dimensions (nm)	Nominal voxel size (µm)	Nominal sampled volume (µm^3)	spatial resolution (µm)
Ga^+ FIB	10 [19]	0.017×0.021×0.2	4×10^3	0.2
Xe^+ PFIB	20-30 [19]	0.036×0.036×0.3	1.9×10^5	0.4
XRT	100 or less [20]	0.87×0.87×0.87	1.6×10^8	4.6

ACKNOWLEDGEMENTS

Siqi He thanks EDF Energy for financial support. Chenge Jiao and ThermoFisher are thanked for their assistance in obtaining the Plasma FIB measurements, whilst J-C and David Cherns are thanked for assistance with STEM and TEM.

REFERENCE

(1) A. D. Warren, *The role of secondary phases in the long term degradation of stainless steels at high temperatures*, PhD thesis, University of Bristol (2015).

(2) P. J. Bouchard, P. J. Withers, S. A. McDonald, and R. K. Heenan, *Acta Mater.* **52,** pp. 23–34 (2004).

(3) A. Yousefiani, F. A. Mohamed, and J. C. Earthman, *Metall. Mater. Trans. A Phys. Metall. Mater. Sci.* **31,** pp. 2807–2821 (2000).

(4) I.-W. Chen and A. S. Argon, *Acta Metall.* **29,** pp. 1321–1333 (1981).

(5) R. G. Fleck, D. M. R. Taplin, and C. J. Beevers, *Acta Metall.* **23,** pp. 415–424 (1975).

(6) A. J. Perry, *J. Mater. Sci.* **9,** pp. 1016–1039 (1974).

(7) B. Chen, P. E. J. Flewitt, D. J. Smith, and C. P. Jones, *Ultramicroscopy*. **111,** pp. 309–313 (2011).

(8) C. Gupta, H. Toda, C. Schlacher, Y. Adachi, P. Mayr, C. Sommitsch, K. Uesugi, Y. Suzuki, A. Takeuchi and M. Kobayashi, *Mater. Sci. Eng. A.* **564,** pp. 525–538 (2013).

(9) T. L. Burnett, R. Geurts, H. Jazaeri, S. M. Northover, S. A. McDoald, S. J. Haigh, P. J. Bouchard and P. J. Withers, *Mater. Sci. Technol.* **31,** pp. 522–534 (2014).

(10) M. Daly, T. L. Burnett, E. J. Pickering, O. C.G. Tuck, F. Léonard, R. Kelley, P. J. Withers and A. H. Sherry, *Acta Mater.* **130,** pp. 56–68 (2017).

(11) T. C. Isabell and V. P. Dravid, *Ultramicroscopy*. **67,** pp. 59–68 (1997).

(12) T. Ishitani and H. Tsuboi, *Scanning*. **19,** pp. 489–497 (2010).

(13) L. A. Giannuzzi and J. R. Michael, *Microsc. Microanal.* **19,** pp. 344–349 (2013).

(14) J. A. Venables, D. J. Smith, and J. M. Cowley, *Surf. Sci.* **181,** pp. 235–249 (1987).

(15) P. R. Munroe, *Mater. Charact.* **60,** pp. 2–13 (2009).

(16) R. E. Franklin, E. C. G. Kirk, J. R. A. Cleaver, and H. Ahmed, *J. Mater. Sci. Lett.* **7,** pp. 39–41 (1988).

(17) E. M. James and N. D. Browning, *Ultramicroscopy*. **78,** pp. 125–139 (1999).

(18) E. Maire and P. J. Withers, *Int. Mater. Rev.* **59,** pp. 1–43 (2014).

(19) T. L. Burnett, R. Kelley, B. Winiarski, L. Contreras, M. Daly, A. Gholinia, M. G. Burke and P. J. Withers, *Ultramicroscopy*. **161,** pp. 119–129 (2016).

(20) S. R. Stock, *Int. Mater. Rev.* **53,** pp. 129–181 (2008).

(21) C. Liu, P. J. Heard, O. D. Payton, L. Picco and P. E. J. Flewitt, *in press.*

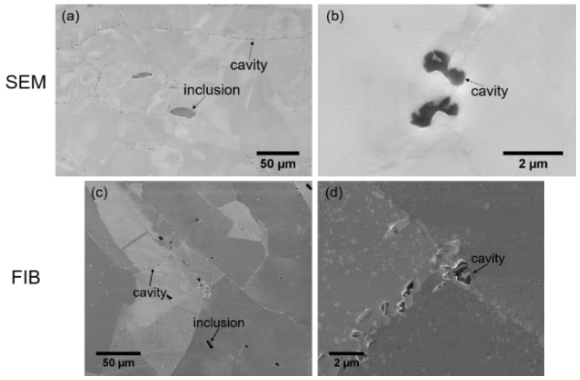

Fig. 1. (a) SEM secondary-electron imaging showing cavities and inclusions; (b) higher magnification SEM showing cavities; (c) and (d) FIB imaging for comparison with SEM.

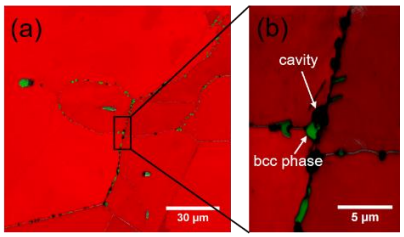

Fig. 2. EBSD phase maps combined with image quality map; red is austenite, and green is bcc phase.

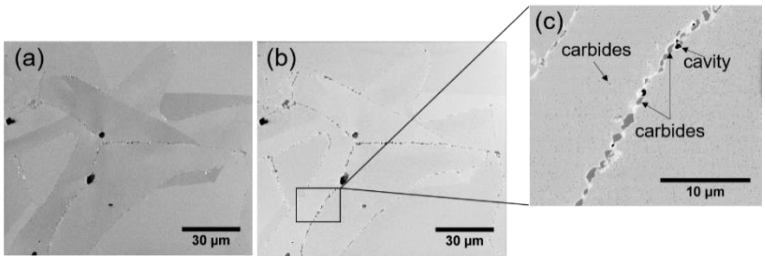

Fig. 3. FIB secondary electron images. (a) before XeF_2 deposition showing strong channelling contrast; (b) after deposition of XeF_2 showing highlighted grain boundaries; (c) zooming in on the grain boundary.

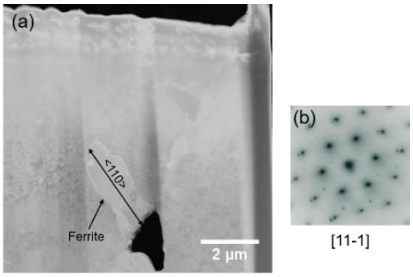

Fig. 4. (a) STEM dark-field imaging showing the cavity and the ferrite at grain boundary; (b) the [11-1] zone axis electron diffraction pattern of the BCC Ferrite.

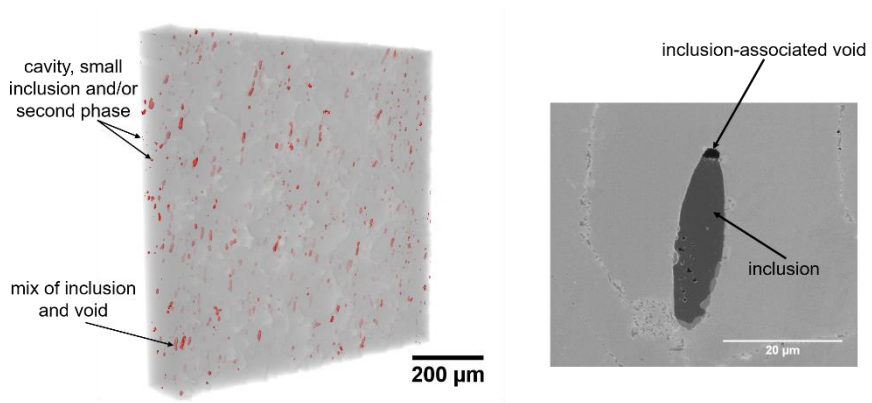

Fig. 5. (a) The reconstructed volume of the XRT scanning with a voxel size of 0.87 µm showing the mix of inclusion and void, grain boundary cavities and/or second phase in the specimen; (b) FIB secondary electron imaging shows the inclusion and inclusion-associated void.

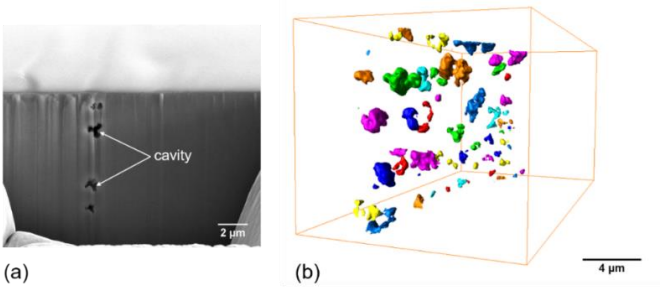

Fig. 6. (a) one slice of the conventional Ga^+ dual beam cross sectioning showing the cavities at the grain boundary; (b) the 3D reconstruction of the creep cavities based on the serial cross-sectioning slices.

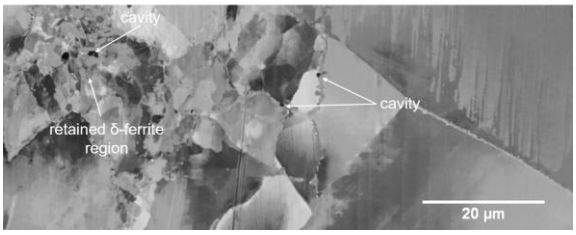

Fig. 7. One frame of the Xe^+ Plasma FIB serial sectioning showing the creep cavities and retained δ-ferrite region.

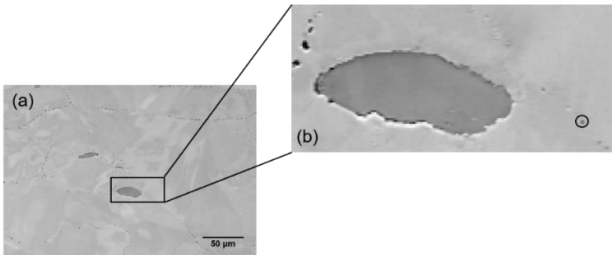

Fig. 8. (a) 1000X magnification SEM image of a typical specimen containing inclusions, voids and cavities; (b) zoom-in image showing the circled feature containing four pixels that is too small to be successfully identified as a cavity.